

CFD simulation of a large-scale VAWT

Evaluation of the rotor performance for a gradient wind profile

Master's thesis in Innovative and Sustainable Chemical Engineering

Mikaela Boberg

Department of Mechanics and maritime sciences
CHALMERS UNIVERSITY OF TECHNOLOGY
Gothenburg, Sweden 2019

MASTER'S THESIS 2019:70

CFD simulation of a large-scale VAWT

Evaluation of the rotor performance for a gradient wind profile

MIKAELA BOBERG



CHALMERS
UNIVERSITY OF TECHNOLOGY

Department of Mechanics and maritime sciences

Division of Fluid dynamics

CHALMERS UNIVERSITY OF TECHNOLOGY

Gothenburg, Sweden 2019

CFD simulation of a large-scale VAWT
Evaluation of the rotor performance for a gradient wind profile
MIKAELA BOBERG

© MIKAELA BOBERG, 2019.

Supervisor: Daniel Grönberg, ALTEN Sverige AB
Examiner: Lars Davidsson, Mechanics and maritime sciences

Master's Thesis 2019:70
Department of Mechanics and maritime sciences
Division of Fluid dynamics
Chalmers University of Technology
SE-412 96 Gothenburg
Telephone +46 31 772 1000

CFD simulation of a large-scale VAWT
Evaluation of the rotor performance for a gradient wind profile
MIKAELA BOBERG
Department of Mechanics and maritime sciences
Chalmers University of Technology

Abstract

SeaTwirl is a developer of a large-scale vertical axis wind turbine and in previous aerodynamic studies of the rotor performance a uniform wind profile have been used. However, the characteristics of the landscape result in friction for the wind flow and the shear stresses generates a gradient wind profile. Hence, this study aims to investigate how the velocity gradients affect the rotor performance and how the efficiency may be increased by alternating the rotor design such as elevating the rotor position or the blade height. The numerical domain consisted of a 2D horizontal cross-section of three airfoils, the tower and struts were excluded. The $k-\omega$ SST turbulence model was used to solve the unsteady RANS equations.

The result showed that the difference in estimated power generation between the usage of a uniform compared to a gradient wind profile deviated with 5%. The result also indicated that it was more beneficial to increase the rotor swept area instead of increasing the rotor position. The study showed that the tip-speed-ratio drastically affected the forces acting on the blades and that these effects are prominent for large-scale vertical axis wind turbines due to the fixed blade configuration. This method was a good implement to obtain a deeper knowledge of the forces acting over the whole blade length. However, performing a full 3D model of the wind turbine would be desirable to validate the 2D method.

Keywords: Vertical axis wind turbine, wind shear, gradient wind profile, CFD

Preface

This master thesis has been performed by Mikaela Boberg at ALTEN Sverige in collaboration with SeaTwirl and the Department of Mechanics and Maritime sciences at Chalmers University of Technology. Daniel Grönberg has been the supervisor at ALTEN Sverige and Lars Davidsson the examiner at Chalmers.

Acknowledgements

I would like to thank my supervisor Daniel Grönberg at ALTEN for his guidance and support regarding CFD. I would like to thank SeaTwirl and especially Jonas Boström who has been their contact person and supporting me with product specific questions. Finally, I would like to thank my examiner Lars Davidsson.

Mikaela Boberg, Gothenburg, June 2019

Contents

List of Figures	xi
List of Tables	xiii
List of Symbols	xiii
1 Introduction	1
1.1 Objective	2
1.2 Demarcations	2
1.3 Methodology	3
2 Theory	5
2.1 Fundamentals of wind energy	5
2.1.1 Wind energy conversion	5
2.1.2 Characteristics of a Vertical Axis Wind Turbine	6
2.1.3 Case specific information	7
2.2 Meteorology	8
2.2.1 Wind regimes	8
2.2.2 Surface roughness	9
2.2.3 Wind profile	9
2.3 Fluid dynamics	10
2.3.1 Governing equations of conservation	10
2.3.2 Turbulence modeling	11
2.3.2.1 The $k-\varepsilon$ model	12
2.3.2.2 The $k-\omega$ model	13
2.3.2.3 The SST $k-\omega$ model	13
2.3.2.4 Near wall modeling	13
3 Simulation	15
3.1 Wind profile generation	15
3.1.1 Logarithmic law and power law	16
3.2 Wind turbine simulation	16
3.2.1 Computational domain and grid	17
3.2.2 Numerical settings	18
4 Results	21
4.1 Generation of a gradient wind profile	21

Contents

4.2	Case set-up	23
4.3	The effect of a gradient velocity profile	25
4.3.1	Power output based on a free stream velocity of 11 m/s	26
4.3.2	Power output based on a free stream velocity of 8 m/s.	27
4.3.3	Forces acting on the blades	30
5	Discussion	35
6	Conclusion	37

List of Figures

2.1	The forces and velocities acting on a three bladed VAWT.	6
2.2	Rotational speed of the turbine versus the measured free stream velocity at hub-height.	8
3.1	Illustration of how the velocity gradients change over the rotor height for a large-scale VAWT.	16
3.2	An illustration of the 2D domain.	17
3.3	Grid configuration on some levels of the domain; (a) Whole numerical domain, (b) Rotating domain with refined mesh, (c) Smaller circles with refined mesh around each airfoil, (d) Close-up of the trailing edge of one blade.	18
4.1	Comparison of wind profiles generated by three different methods. . . .	21
4.2	History effect of the averaged power coefficient.	24
4.3	The torque coefficient for the different free stream velocities at different heights.	25
4.4	The resulting C_{pavg} for the different free stream velocities at different heights.	25
4.5	The left graph illustrates the calculated power at different heights. The right graph illustrates the total power output for the current rotor design.	26
4.6	The graphs display the total power output for positioning the rotor 10 m higher (left) and 20 m higher (right) than current design.	27
4.7	The graphs display the total power output for 45 m tall (left) and 50 m tall (right) rotor blades.	27
4.8	The graphs displays the power curve for a free stream velocity of 8 m/s (left) where the total power output for the rotor is given by the area under curve (right).	28
4.9	The graphs displays the total power output for positioning the rotor 10 m higher (left) and 20 m higher (right) compared to current design. . .	28
4.10	The graphs displays the total power output if the rotor blades would be 45 m (left) and 50 m (right).	29
4.11	Variation in angle of attack during one blade revolution for different tip-speed-ratios.	30
4.12	Lift coefficient for one blade versus azimuthal angle of attack for three different tip-speed-ratios.	31
4.13	Lift coefficient for one blade versus angle of attack.	31
4.14	Drag coefficient for one blade over one revolution.	32

List of Figures

4.15 Drag coefficient for one blade versus angle of attack. 32

4.16 Contour plots of vorticity magnitude illustrating the flow separation for
different tip-speed-ratios at an azimuthal angle of 130° and 150°. 33

List of Tables

2.1	Typical values of the roughness length for different landscapes. [1] . . .	9
3.1	Differences between the four constructed meshes.	18
4.1	Derived velocities and tip-speed-ratios for two different free stream velocities at hub-height.	22
4.2	Deviation in the power coefficient for meshes with different refinement of cells.	23
4.3	Deviation in power coefficient for different azimuthal increments per time step.	24

List of Symbols

α	Power law exponential
Δt	Time step size
λ	Tip-speed-ratio
μ	Dynamic viscosity
ν	Kinematic viscosity
ω	Rotational speed
ρ	Air density
τ	Shear stress
θ	Azimuthal angle
ε	Turbulent dissipation rate
A_T	Rotor swept area
AOA	Angle of attack
c	Chord length
C_D	Drag coefficient
C_L	Lift coefficient
C_P	Power coefficient
C_T	Torque coefficient
D	Rotor diameter
E	Empirical constant
g	Body forces
H	Rotor blade height
h_m	Kinetic energy
i, j, k	Directions
k	Turbulent kinetic energy
K_s	Roughness height
P	Power, Pressure
R	Rotor radius
T	Torque

List of Tables

t	Time
U	Velocity
u^*	Friction velocity
W	Relative velocity
y	First cell wall distance
y^+	Dimensionless wall distance
z	Height
z_0	Roughness length
κ	von Kármán constant

1

Introduction

Extracting energy from the wind has been utilized for several years, but still there is research on new configurations and creative solutions to extract this sustainable energy. However, no processes are uncomplicated and satisfyingly efficient. There is always room for improvement, whether its improving old ideas or discover new ones.

Vertical axis wind turbines, VAWT, began to be developed during the early 20th century. The *Darrieus rotor*, the foundation of modern VAWT's rotor design, was designed by the French engineer Darrieus and patented in 1931. It was first designed as a *troposkein*, two blades formed as an egg, but due to difficulties with manufacturing the more simple H-rotor with straight blades was developed. A few large scale projects have been conducted over the years. During the eighties the largest troposkein, with an estimated power generation of 4 MW, was built in the so called *Eóle* project. In the same era a German manufacturer was producing commercial H-rotors with an estimated power generation of 300 kW. Unfortunately, those projects were terminated due to the tough competition with horizontal axis wind turbines. [2]

There are several major differences between the designs of a horizontal versus vertical axis wind turbine. First of all, the hub which is the housing of the mechanical components, is placed at ground level instead of high up in the air. This is favourable since this simplifies the construction of the tower and the maintenance of the mechanical parts. Another advantage for the VAWT is the elimination of a yaw system, since the wind direction is always perpendicular to the swept area. [3] However, due to the vertical rotation, the angle of attack for the airfoils are constantly changing during one revolution. As a result the overall lift force is reduced which leads to lower efficiency compared to horizontal axis wind turbines. Besides, the fixed rotor blades make them unable to control the rotational speed by blade pitching movement, as well as making the rotor unable to self-start. [2]

The design of vertical axis wind turbines can be alternated into eternity with all creative configurations. Due to the various designs the power output differs for each turbine and the efficiency is characterized by the power coefficient, C_p , which is defined as the ratio between the power generated by the rotor and the theoretical available energy in the wind. The power coefficient varies with the tip-speed-ratio and in turn, this relation depends on several rotor design parameters. Thus, for every turbine design the optimal relation between power coefficient and tip-speed-ratio needs to be determined to be able

to optimize the efficiency. Numerical investigation by computational fluid dynamics is a common approach to find the optimal tip-speed-ratio for maximum turbine performance. Most of the existing numerical studies are conducted for small-scale VAWTs where the diameter of the rotor is around 1 m. Especially prominent is the work done by Marco Raciti Castelli, which is cited in the majority of the studies. Common applications for small-scale vertical axis wind turbines is in urban environments but for power generation large-scale designs are required and numerical studies on large-scale VAWTs are scarce.

SeaTwirl is a Swedish developer of large-scale floating off-shore vertical axis wind turbines. Their design concept consist of a three bladed Darrieus rotor, a tower and a keel below the water surface that contributes with stability. The wind turbine is constructed such that the rotor, tower and keel are rotating as one part, while the generator housing is fixed and anchored to the seabed. Their latest model SeaTwirl S2, with a rotor diameter of 50 m and blade height of 40 m, is under development and some design parameters are to be examined in this project.

In their previous studies of the rotor performance a uniform wind profile has been used. Nevertheless, in reality the wind profile is far from uniform due to the shear stresses that are built up by the roughness length of the landscape. For a large-scale VAWT with a significant blade height, the wind shear is expected to affect the power output and the forces acting over the blade height.

1.1 Objective

The aim of this project is to represent how the power generation for a large-scale vertical axis wind turbine is affected by the velocity gradients. The first objective is to find the optimal method to generate a realistic wind profile. Thereafter, the objective is to perform simulations on SeaTwirl's wind turbine model and find out how the power output will change with increased height above the sea surface. Based on the results, design parameters that could improve the power extraction will be investigated, such as the position of the rotor or the height of the rotor blades. Accordingly, the research questions are:

- How is a realistic velocity profile generated?
- How is the power output influenced by the wind shear?
- How is the power output improved by changing the design such as increasing the rotor position or the blade height?

1.2 Demarcations

This study is simplified such as only the rotor blades are being studied and thus the struts, the tower and the keel are neglected. Neither is the movement of the turbine due to wave motion relevant. The study is simplified to 2D simulations which represent

a horizontal cross-section of the rotor. As a result, 3D effects and losses due to tip vortices is not included. It also means that no validation of the 2D predictions reliability is available, for that a full 3D model would be needed. Regarding environmental circumstances the study assumes constant weather conditions, which eliminates fluctuating wind speed, influence on the surface roughness due to history of the waves and constant density of the air. Due to confidentiality the model and dimensions of the airfoils will not be mentioned.

1.3 Methodology

The software ANSA will be used to construct and mesh the 2D models. The numerical studies will be performed in the software Ansys Fluent 17. The results of the turbine performance will be compared to previous studies performed at ALTEN Sverige for SeaTwirl.

This chapter covers some general information about power extraction by wind engineering and vertical axis wind turbines. Then, a short introduction in meteorology and why it is of relevance to include velocity gradients when evaluating the rotor performance by numerical analysis. Finally, the numerical theory is introduced, where the current methods available are presented and what limitations and assumption they include.

2.1 Fundamentals of wind energy

2.1.1 Wind energy conversion

Power is generated by the kinetic energy in the wind and the theoretical amount of power that can be extracted by the kinetic energy is described with equation 2.1, where A_T is the swept area of the rotor, and U_∞ is the free stream velocity magnitude of the wind. As can be seen, the essential factors for wind power extraction is the swept area and the velocity of the wind, which is of the power to three.

$$P = \frac{1}{2}\rho A_T U_\infty^3 \quad (2.1)$$

However, no system is ideal and the amount of power extracted from the available kinetic energy depends on the wind turbine design. The efficiency can be stated by the power coefficient, C_p , equation 2.2, which describes the ratio between the power generated by the rotor, P_T , and the theoretical available energy. A well known theory is the *Betz limit*, which propose that for a horizontal axis wind turbine, the theoretical maximum value of the power coefficient is 59.3 %. [3] This is expected to be lower for vertical axis wind turbines due to shortcomings of the design, which are described in the following section.

$$C_p = \frac{P_T}{\frac{1}{2}\rho A_T U_\infty^3} \quad (2.2)$$

To optimize the power generation for a turbine, one important factor is the relation between the tip speed of the blades and the incident wind velocity which is called the tip-speed-ratio, λ , equation 2.3. The tip speed depends on the rotor radius, R , and the rotational velocity of the rotor, ω . Thus, for all rotor models, it's essential to find the tip-speed-ratio which results in the maximum power extraction.

$$\lambda = \frac{R\omega}{U_\infty} \quad (2.3)$$

2.1.2 Characteristics of a Vertical Axis Wind Turbine

A major difference for a vertical axis wind turbine compared to a horizontal axis turbine, is that the angle of attack is constantly changing during one revolution. A blade is exposed to the incoming wind for 0° to 180° ; then it moves in the shadow of another blade and is subjected to a lower amount of kinetic energy.

Therefore, one blade experiences both positive and negative torque as it travels through one revolution. As a result, the total energy extraction is lower than for a horizontal axis wind turbine. [2]

The aerodynamics of a three bladed VAWT is depicted in figure 2.1, where the relative velocity, W , is the vector sum from the incoming velocity and the tangential velocity, equation 2.4. The angle of attack, AOA, which changes during the revolution and is dependent on the tip-speed-ratio, is derived by equation 2.5.

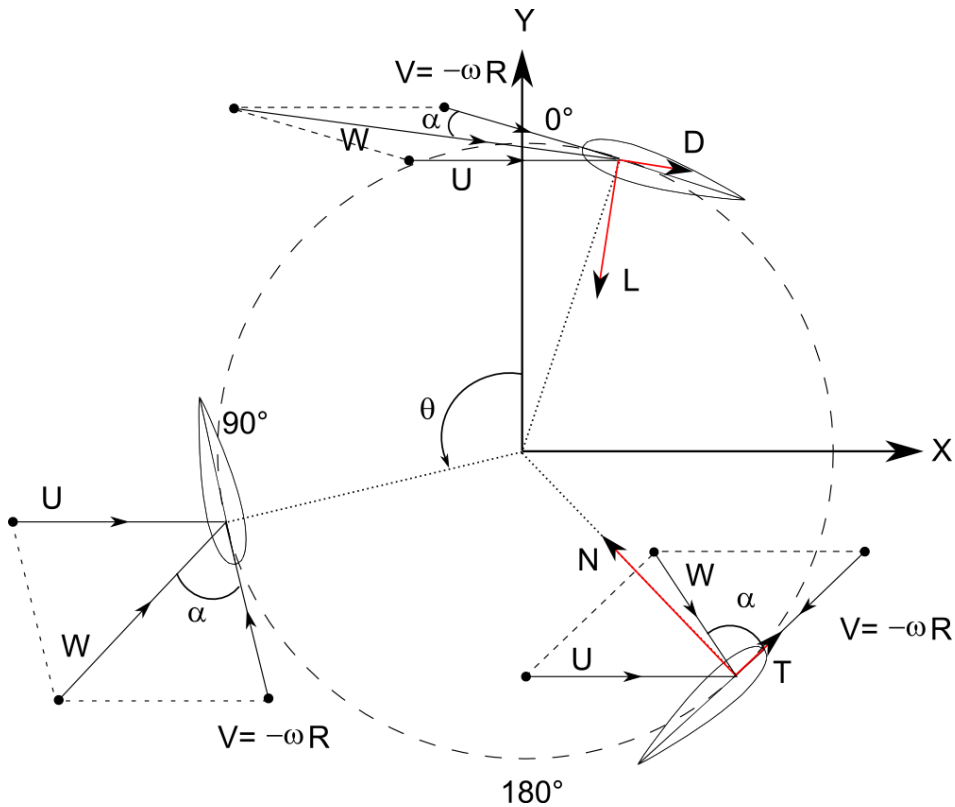


Figure 2.1: The forces and velocities acting on a three bladed VAWT.

$$W = U_\infty \sqrt{\sin^2\theta + (\lambda + \cos\theta)^2} \quad (2.4)$$

$$AOA = \tan^{-1}\left(\frac{\sin\theta}{\lambda + \cos\theta}\right) \quad (2.5)$$

From the numerical analysis the forces in X- and Y-direction are obtained. These are later on used to calculate the lift and drag coefficients for each azimuthal angle according to equation 2.6 and 2.7, where c is the chord length and F_x and F_y is the forces in X- and Y-direction.

$$C_L(\theta) = \frac{F_x[\sin(\theta - \alpha)] - F_y[\cos(\theta - \alpha)]}{\frac{1}{2}\rho cHW^2} \quad (2.6)$$

$$C_D(\theta) = \frac{F_x[\cos(\theta - \alpha)] + F_y[\sin(\theta - \alpha)]}{\frac{1}{2}\rho cHW^2} \quad (2.7)$$

The torque coefficient, $C(\theta)$, is derived by equation 2.8, where the total torque, $T(\theta)$ as a function of azimuthal angle, is given by the tangential force and rotor radius. For a vertical axis wind turbine, the swept area A_T , is determined by the rotor radius and the height of the blades, according to equation 2.9. In this project the rotor radius is 25 m. In 2D numerical analysis the height of the blades are specified as 1 m. By the averaged torque coefficient and the tip-speed-ratio, the power coefficient is determined, equation 2.10. Thereafter the total power output is calculated by equation 2.2.

$$C_T(\theta) = \frac{T(\theta)}{\frac{1}{2}\rho A_T U_\infty^2 R} \quad (2.8)$$

$$A_T = 2RH \quad (2.9)$$

$$C_p = C_T \lambda \quad (2.10)$$

2.1.3 Case specific information

The diameter of the rotor is 50 m and the total blade height is 40 m, which result in a swept area of 2000 m². The free stream velocity of the incoming wind is measured at hub-height which is located 35 m above the sea surface. The cut in speed, which is when the power production starts, is 4 m/s. Between 4 m/s to 10 m/s the rotational speed of the turbine is operated to give a tip-speed-ratio of 3, see Figure 2.2. Between 10 m/s and the cut-out speed, which is 22 m/s, the rotational speed is kept close to 1.2 rad/s.

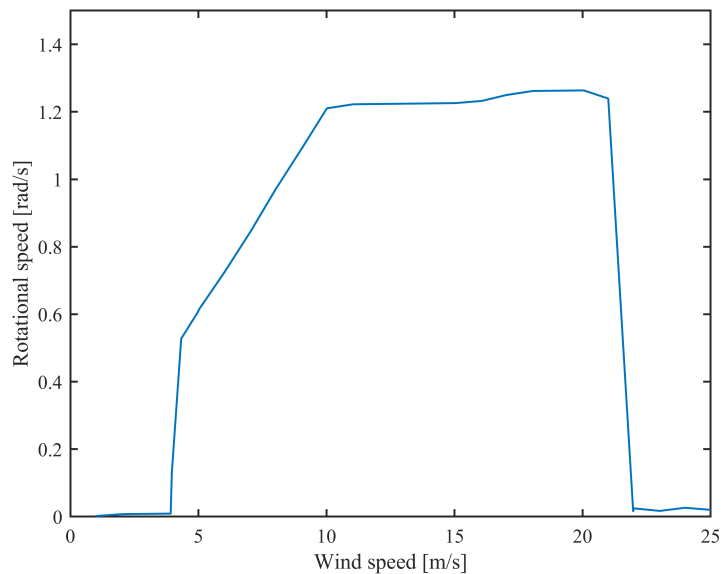


Figure 2.2: Rotational speed of the turbine versus the measured free stream velocity at hub-height.

2.2 Meteorology

Information of the intended location of the wind turbine can help to predict the possible energy extraction since the wind flow is affected by the characteristics of the landscape.

2.2.1 Wind regimes

The lowest region of the Earth's atmosphere is called the atmospheric boundary layer, *ABL*, and it reaches from the planetary surface up to 1 km. The *ABL* is divided into three layers, where the region closest to the surface is laminar and only a few millimeters thick. The next region is the surface layer, also called the Prandtl layer, whose height depends on the characteristics of the planetary surface and thermal stratification. In marine environment, such as a flat open sea, the height of the Prandtl layer ranges from 10-100 m, while over more complex terrain with large obstacles such as cities, it can range up to 450 m. Since the Prandtl layer has contact with the ground surface it is subjected to shear stresses that slow down the flow, which generates vertical velocity gradients. Hence, a variation in velocity is observed over height. The rest of the *ABL* consists of the Ekman layer and this regime is affected by the Earth's rotation. Hence, the contribution of the Coriolis force, which causes a turning of wind direction with height, needs to be accounted for in the wind profile. Therefore, a mathematical description of the wind profile in the Ekman layer is much more complex than for the Prandtl layer. Since the total height of the vertical axis wind turbine in this study is below 100 m, only the Prandtl layer has been considered.

Horizontal temperature gradients, thermal winds, are an important driving force when the surface friction is low, which is the case for open sea. To account for the vertical

heat flux a stability-correction function is needed. [4] However, thermal contribution has not been considered in this project and thus the governing equations can be simplified considerably. [1] Instead the equations used in this project are derived for neutral stratification.

2.2.2 Surface roughness

The characteristics of the landscape result in different magnitude of surface friction. Large obstacles like buildings, mountains and high vegetation result in significant surface roughness that generates much wind shear. While agricultural land, grass, desert, ocean and similar flat terrains result in less surface roughness. The surface roughness is classified by the roughness length, which is the height above the surface where the mean wind velocity theoretically should be zero. Table 2.1 displays a few general classifications of roughness lengths. [1] [4] In contrast to the mainland, the roughness length of the ocean is particularly complex since it is constantly changing. It is dependent on the current weather conditions, the stability of the stratification and the history of the waves. The wind shear, that arises from the surface roughness, generates turbulence. The offshore turbulence intensity is often in the range of 5 to 10 %. [1]

Table 2.1: Typical values of the roughness length for different landscapes. [1]

Terrain	Roughness length z_0 [m]
Open flat sea	0.0001
Open rough sea	0.001
Open country without significant buildings and vegetation	0.03
Cultivated land with scattered buildings	0.05
Forest and suburbs	0.3-0.5
Cities with tall buildings	1-5
Mountains	1-5

2.2.3 Wind profile

A gradient velocity profile can be imitated either by the empirical power law or by the more theoretical logarithmic law. In this project neutral stratification has been assumed, hence eliminating the effect of atmospheric stability conditions due to thermal stratification, resulting in the simplified logarithmic law defined in equation 2.11. [1] Where z_0 is the roughness length of the landscape given in table 2.1, z is the height above the surface, κ is the Von Kármán constant which is $\kappa=0.41$ and u^* is the friction velocity which can be calculated by equation 2.12. The friction velocity is a function of the wall shear stress τ and the air density ρ .

$$u(z) = \frac{u^*}{\kappa} \ln \left(\frac{z}{z_0} \right) \quad (2.11)$$

$$u^* = \sqrt{\frac{\tau}{\rho}} \quad (2.12)$$

The expression for the power law is based on Prandtl's one-seventh power law, where the exponential α depends of the surface roughness and thermal stability, but for neutral stratification the value of α is 0.143 i.e 1/7. The known free stream velocity, u_{z_r} , at a reference height, z_r , is used to calculate the velocity at any other height.

$$u(z) = u_{z_r} \left(\frac{z}{z_r} \right)^\alpha \quad (2.13)$$

2.3 Fluid dynamics

Fluid dynamics is the description of the physical phenomena that appears for a flow in motion. It describes the forces acting on the fluid and how energy is transferred.

2.3.1 Governing equations of conservation

A mathematical description of the motion of a fluid can be done by the laws of conservation. These are the conservation of mass, Newton's second law of motion which is the conservation of momentum and finally the first law of thermodynamics which describes the conservation of energy. The fluid properties cannot be destroyed, but can be changed into other forms of energy. For single-phase flow, the continuum assumption is a requirement, which applies a separation of scales so that the smallest scale occurring in the flow are still far larger than the molecular length scale. Hence, physical phenomena that occur on molecular level, like random movement and collisions of molecules, are not included in the mathematical description. [5]

The conservation equations describe the rate of change over a system, where the flux in and out of the control volume equals the accumulation inside. Hence, the differential form of change of mass over a system is described as:

$$\frac{\partial \rho}{\partial t} + \frac{\partial \rho U_j}{\partial x_j} = 0 \quad (2.14)$$

Whereas the change in density is equal to the net flux over the system boundaries. For incompressible flow, where no change in density occur because ρ is constant, the equation is simplified such as the net flux in and out of the system is equal to zero.

The equation of motion are described by the rate of change of momentum to and from the system which should be equal the forces acting on the system. Forces that may affect the system are surface forces like pressure and viscous forces, body forces like gravity or electrical forces.

$$\frac{\partial U_i}{\partial t} + U_j \frac{\partial U_i}{\partial x_j} = -\frac{1}{\rho} \frac{\partial P}{\partial x_i} + \frac{1}{\rho} \frac{\partial \tau_{ji}}{\partial x_j} + g_i \quad (2.15)$$

The conservation of energy implies that the rate of change of energy is equal to the heat or work added to the system. The energy may be transformed into different forms such as kinetic, thermal, chemical or potential energy; however, the total energy should remain constant. The conservation equation for mechanical energy reads:

$$\frac{\partial h_m}{\partial t} = -U_j \frac{\partial(h_m)}{\partial x_j} + P \frac{\partial U_i}{\partial x_i} - \frac{\partial(PU_i)}{\partial x_i} + \frac{\partial}{\partial x_j}(\tau_{ij}U_i) + \tau_{ij} \frac{\partial U_i}{\partial x_j} + \rho g_i U_i \quad (2.16)$$

The term on the left-hand side stand for accumulation of energy. On the right-hand side the first term stands for convection, the second term for reversible conversion of heat, the third term for rate of work done by the surroundings, the fourth term for the work done by viscous forces, the fifth term stands for irreversible conversion to heat and the last term is for work done by gravity force. [6]

Viscous stresses arise from friction between the moving fluid and a surface, which causes a deformation of the fluid over time. The deformation of fluids such as air and water, can be approximated by the linear strain rate function and are therefore called Newtonian fluids. Fluids whose deformation does not follow the linear strain rate is called non-Newtonian fluids. The viscous stresses consist of shear stresses, τ_{ij} that are proportional to the velocity gradient, according to equation 2.17. The normal stresses, τ_{ii} are simplified for incompressible flows and the resulting viscous stress are described by equation 2.18. [7]

$$\tau = \mu \frac{du}{dy} \quad (2.17)$$

$$\tau_{ij} = \mu \left(\frac{\partial U_i}{\partial x_j} + \frac{\partial U_j}{\partial x_i} \right) \quad (2.18)$$

2.3.2 Turbulence modeling

Turbulent flow is characterized by the random and fluctuating movement of the fluid and is constantly changing with time. In turbulent flow, energy is transferred by turbulent structures that are called turbulent eddies. The turbulent eddies have different length and timescales depending on how much kinetic energy they are containing. Turbulent eddies are produced by the energy from the mean flow and thereafter broken up into smaller structures, which yield a constant energy flux from larger length scales down to the smaller scales. Since the turbulent structures are broken down, there is a decay of turbulence over time. When the smallest scale of turbulent eddies, the *Kolmogorov scale* is reached, the eddies are destroyed and the contained energy is dissipated into heat. [6]

The complex physical behaviour of turbulent flow can be approximated by decomposing the flow variables into a time-averaged mean and a fluctuating part, according to equation 2.19, and is called the Reynolds decomposition. The intensity of the velocity fluctuations are described as turbulent kinetic energy, equation 2.20. [6]

$$U_i = \langle U_i \rangle + u_i \quad (2.19)$$

$$k = \frac{1}{2} \langle u_i u_i \rangle \quad (2.20)$$

The Reynolds decomposition is used to solve the governing equations for turbulent flow, hence the resulting Reynolds-averaged Navier-Stokes, *RANS*, for the momentum equation reads;

$$\frac{\partial \langle U_i \rangle}{\partial t} + \langle U_j \rangle \frac{\partial \langle U_i \rangle}{\partial x_j} = -\frac{1}{\rho} \frac{\partial \langle P \rangle}{\partial x_i} + \nu \frac{\partial^2 \langle U_i \rangle}{\partial x_j^2} - \frac{\langle \partial u_i u_j \rangle}{\partial x_j} \quad (2.21)$$

In the RANS equation the Reynolds stress tensor, equation 2.22, is introduced. It is a fictitious term that represents the interaction between the turbulent eddies and the mean flow. The tensor is symmetric, τ_{ij} is equal to τ_{ji} , which results in six unknown variables that requires modelling and is commonly known as the closure problem. [6] These quantities may be modelled by correlation with other known physical quantities, thus, the RANS equations would be possible to solve without adding extra equations. [5] The Boussinesq approximation is a closure that relates the momentum transport with diffusion and correlates the stress components to the mean velocity gradients. Turbulent viscosity is introduced, which is analogous to molecular viscosity, although it is not a fluid property but a local description of the flow. Hence, the Boussinesq approximation assumes that the turbulent eddies behaves as molecules. [6]

$$\tau_{ij} = -\rho \langle u_i u_j \rangle \quad (2.22)$$

$$\frac{\tau_{ij}}{\rho} = -\langle u_i u_j \rangle = \nu_T \left(\frac{\partial \langle U_i \rangle}{\partial x_j} + \frac{\partial \langle U_j \rangle}{\partial x_i} \right) - \frac{2}{3} k \delta_{ij} \quad (2.23)$$

With the Reynolds stress tensor as closure for the production of k , the turbulence energy equation can be derived, equation 2.24. This transport equation of kinetic energy is the foundation for all two-equation turbulence models. The terms on the left-hand side stand for accumulation and convection of k , the first and second terms on the right-hand side stand for production of k and dissipation of k respectively, where the turbulent dissipation rate per unit mass, ε , is unknown and defined by equation 2.25. [6] The last terms represent turbulent transport and pressure diffusion, and an assumption is to model them as a gradient-diffusion transport mechanism. The turbulent viscosity ν_T is closed according to equation 2.26 where the coefficient C_μ is equal to 0.09. The coefficient σ_k is a model constant of unity. [6]

The turbulent kinetic energy equation is not fulfilled until the turbulent viscosity and the turbulent dissipation rate is solved. The turbulent dissipation rate requires a separate transport equation which can be formed in several ways.

$$\frac{\partial k}{\partial t} + \langle U_j \rangle \frac{\partial k}{\partial x_j} = \tau_{ij} \frac{\partial \langle U_i \rangle}{\partial x_j} - \varepsilon + \frac{\partial}{\partial x_j} \left[\left(\nu + \frac{\nu_T}{\sigma_k} \right) \frac{\partial k}{\partial x_j} \right] \quad (2.24)$$

$$\varepsilon = \nu \left\langle \frac{\partial u_i}{\partial x_j} \frac{\partial u_i}{\partial x_j} \right\rangle \quad (2.25)$$

$$\nu_T = C_\mu \frac{k^2}{\varepsilon} \quad (2.26)$$

2.3.2.1 The k- ε model

One of the most well-known turbulence model is the k- ε model. The derivation of the turbulent dissipation rate is complex and contributes to more unknown variables.

Therefore, additional model constants are introduced to simplify the final expression. Thus, the turbulent dissipation rate can be modelled according to equation 2.27, where the two terms on the left-hand side stand for accumulation and convection of ε by the mean flow. [6] The first term on the right-hand side stands for production of ε which contains a closure constant $C_{\varepsilon 1}=1.44$. The second term is dissipation of ε which also contains a closure constant, $C_{\varepsilon 2}=1.92$. The last term on the right-hand side stands for diffusion of ε where the closure coefficient σ_ε is equal to 1.30.

Since the k- ε turbulence model is derived from the eddy-viscosity assumption it is limited to isotropic flows and therefore has difficulties to deliver accurate results for flows that contain strong curvature and swirls. [6]

$$\frac{\partial \varepsilon}{\partial t} + \langle U_j \rangle \frac{\partial \varepsilon}{\partial x_j} = C_{\varepsilon 1} \nu_T \frac{\varepsilon}{k} \left[\left(\frac{\partial \langle U_i \rangle}{\partial x_j} + \frac{\partial \langle U_j \rangle}{\partial x_i} \right) \frac{\partial \langle U_i \rangle}{\partial x_j} \right] - C_{\varepsilon 2} \frac{\varepsilon^2}{k} + \frac{\partial}{\partial x_j} \left[\left(\nu + \frac{\nu_T}{\sigma_\varepsilon} \right) \frac{\partial \varepsilon}{\partial x_j} \right] \quad (2.27)$$

2.3.2.2 The k- ω model

Another way to define the turbulent dissipation rate is by unit time, as opposed to unit mass which was the definition for ε . [5] Thus, the specific dissipation rate, ω , is obtained and related to ε according to $\omega \sim \varepsilon/k$. The turbulence viscosity is then defined as equation 2.28 and the transport equation for the specific dissipation rate is defined by equation 2.29. The k- ω turbulence model is capable to predict the turbulence in the free stream, as well as in near wall regions; thus no wall functions are needed. Nevertheless, this requires very fine mesh quality in the vicinity of the wall. The first grid point needs to be below a y^+ value of 5. The turbulence model can also deal with low Reynolds number and separated flows. [6]

$$\nu_T = \frac{k}{\omega} \quad (2.28)$$

$$\frac{\partial \omega}{\partial t} + \langle U_j \rangle \frac{\partial \omega}{\partial x_j} = \alpha \frac{\omega}{k} \nu_T \left[\left(\frac{\partial \langle U_i \rangle}{\partial x_j} + \frac{\partial \langle U_j \rangle}{\partial x_i} \right) \frac{\partial \langle U_i \rangle}{\partial x_j} \right] - \beta^* \omega^2 + \frac{\partial}{\partial x_j} \left[\left(\nu + \frac{\nu_T}{\sigma_\omega} \right) \frac{\partial \omega}{\partial x_j} \right] \quad (2.29)$$

2.3.2.3 The SST k- ω model

This turbulence model utilizes the favourable methods from the two previous models. The k- ε model is used to describe the turbulence in the free stream while the k- ω turbulence model describes the turbulence in the vicinity of the wall. As a result, the model can predict the physics in both the free-stream and in the near wall region, without the use of any wall functions. Nevertheless, the same mesh criterion as for the k- ω model applies.

2.3.2.4 Near wall modeling

In the vicinity of the wall the fluid velocity is slowed down due to surface friction. The shear stresses generates a boundary layer with steep velocity gradients, where the fluid velocity is zero and then grows logarithmic with the distance from the wall. The

boundary layer can be divided into three sub-layers and its total thickness, δ , is the distance from the wall where the velocity has reached 99% of the free stream velocity. The region closest to the surface is the viscous sub-layer where the flow is laminar and the dissipation rate is high due to the viscous stresses. Following, is the buffer sub-layer where both the viscous stresses and the turbulent stresses influence the flow and the production of turbulent kinetic energy reaches its maximum. Further away from the wall, the turbulent stresses become significant while the viscous stresses become negligible, hence the third layer is called the fully-turbulent sub-layer. In this region the production and dissipation rate are equal. [6]

The extent of the sub-layers can be determined by the non-dimensional wall distance y^+ , equation 2.30, where y is the distance from the surface, ν is the kinematic viscosity and u^* is the wall friction velocity defined in equation 2.12. [6]

$$y^+ = \frac{yu^*}{\nu} \quad (2.30)$$

The viscous sub-layer reaches up to a y^+ of 5. Thereafter, for a y^+ in the interval 5-30 is the buffer sub-layer. The fully turbulent sub-layer ranges from a y^+ of 30-400. To be able to resolve the physics that occur in the near wall region a fine resolution of the mesh is needed. [6] Especially the k- ϵ turbulence model has difficulties with describing the physics and requires implementation of a wall function that simplifies the numerical solution.

The concept of wall functions is to exclude the complex physics in the vicinity of the wall. Instead the calculation proceeds with taking values from the first grid point next to the wall and a predefined solution of the viscous region is applied. This is an assumption that may give inadequate results because it depend on the location of the first grid point. The first grid point need to be located in the boundary layer, as close to the buffer-sub layer as possible, i.e $30 < y^+ < 100$. [6]

3

Simulation

This chapter introduces the methods used to perform the numerical studies. To begin with, the wind profile was generated by three different methods. Thereafter, the project continued with setting up a 2D domain of a cross-sectional plane of the wind turbine. Finally 2D simulations, based on the derived velocity gradients, were performed and analyzed.

3.1 Wind profile generation

The landscape of the intended location for the wind turbine is of relevance when generating a wind profile, since the wind flow is formed by the obstacles in the landscape. In this case, the wind turbine should be placed off-shore, hence the roughness length of the sea surface was an essential parameter.

To begin with, a periodic simulation was carried out, where the gradient velocity profile was generated solely by the the wall shear stress at the wall boundary. The numerical domain was constructed as a rectangle with a length of 500 m and a height of 200 m. A structured quadrilateral mesh with cell length of 0.5 m and first cell height of 0.005m was generated. In order of best practice guidelines, the first cell height was chosen to ensure that the distance from the wall to centre of the wall-adjacent cell was higher than the roughness height, K_s . [8] The roughness height was derived according to equation 3.1 where the empirical constant $E=9.793$, the default value of the roughness constant $C_s=0.5$ and the roughness length $z_0=0.0001$, according to table 2.1, were used. Hence, the roughness height was calculated to 0.0019586 m.

The boundary conditions of the numerical domain were set as velocity-inlet, pressure-outlet, wall at the bottom and symmetry on the top.

$$K_s = \frac{Ez_0}{C_s} \quad (3.1)$$

An inlet mass flow of 2842 kg/s was set as periodic condition. The turbulence model used was the steady k- ϵ with standard wall functions. The SIMPLE algorithm was used for the pressure-velocity coupling and second order scheme for spatial discretization. Initial starting values of the turbulent kinetic energy and dissipation rate were set as 0.4.

3.1.1 Logarithmic law and power law

The logarithmic law formula required a known friction velocity and roughness length. For this case the friction velocity was unknown, thus the free stream velocity of 11 m/s at 35 m above the sea surface was used as reference values in equation 2.11 to calculate the friction velocity for that conditions. This resulted in 0.3532 m/s and by that, the velocity gradients over a height of 200 m were derived to construct the wind profile. The power law formula required a known free stream velocity at a reference height. Hence, the free stream velocity was set to 11 m/s at the reference height 35 m in equation 2.13 and the wind profile over 200 m height was generated.

With the information from the velocity profile, the free stream velocities at seven additional heights were achieved. Since the height of the rotor blades ranged from 10 m to 50 m above the sea surface, the velocities at 10 m, 20 m, 20 m, 40 m and 50 m above the sea surface were calculated, illustrated in Figure 3.1. The velocities at 60 m and 70 m were of interest to be able to evaluate the design options.

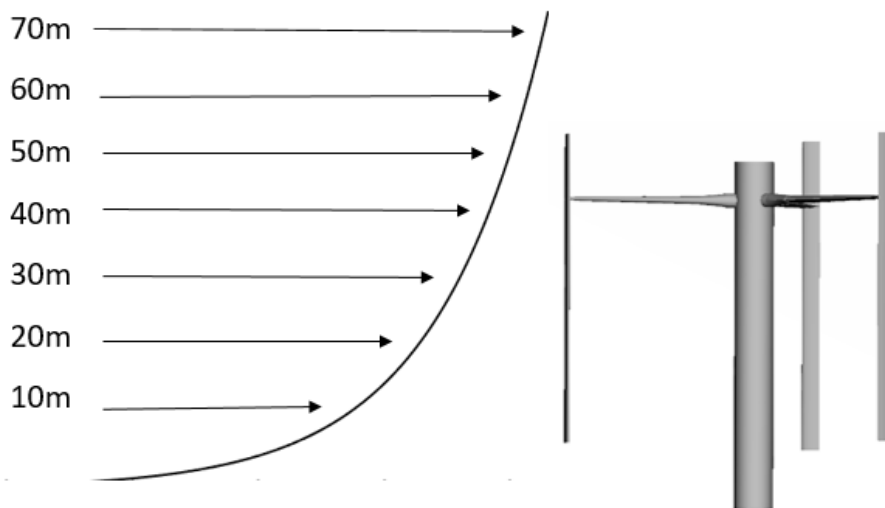


Figure 3.1: Illustration of how the velocity gradients change over the rotor height for a large-scale VAWT.

3.2 Wind turbine simulation

The investigation was carried out by 2D simulations of a cross-sectional plane of the rotor. The inlet velocities were to represent the free stream velocity at a certain height, according to Figure 3.1. First of all, the numerical method was evaluated by investigating parameters that could affect the solution i.e the mesh quality and the time step size. When an optimal numerical method was found, the study went on to investigate the effect of a gradient wind profile on the turbine performance.

3.2.1 Computational domain and grid

The domain consisted of a horizontal cross-sectional plane of the rotor and a simple version of the domain is illustrated in Figure 3.2. According to the coordinate system depicted in Figure 2.1 the starting position for blade 1 is at 0° , blade 2 at 120° and blade 3 at 240° . The dimensions of the domain were specified according to a study performed by Blocken, Rezaeiha and Kalkman (2017) where they recommended a minimum distance from the inlet to the turbine position of $10D$ as well as a minimum distance from turbine position to outlet of $10D$. According to their study a smaller domain size would affect the turbine performance. [9] In their study they also recommended a domain width of $20D$ to minimize the blockage ratio and the risk of artificial acceleration of the flow, however due to computational cost, a domain width of $10D$ was used which resulted in a blockage ratio of 10%. The diameter of the rotating domain was $1.4D$.

The boundary conditions were uniform velocity and pressure-outlet for the inlet and outlet respectively. The sides were set as symmetry and the rotating domain as interface.

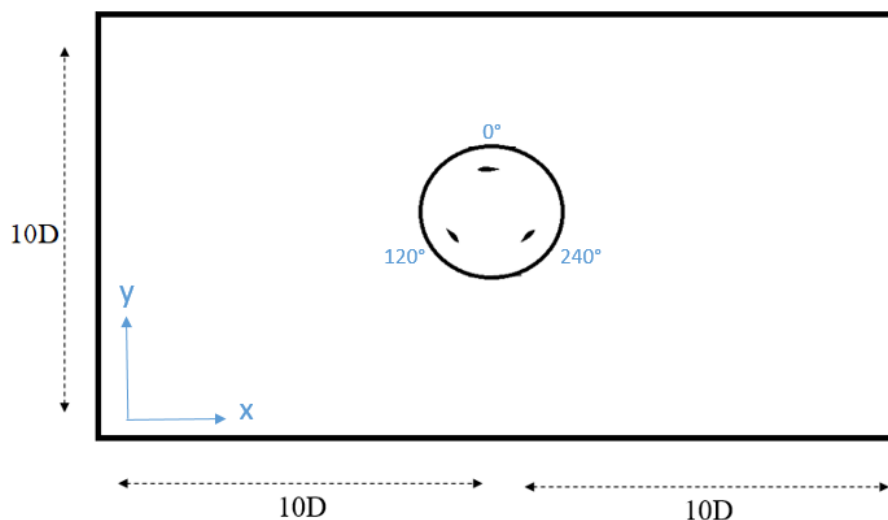


Figure 3.2: An illustration of the 2D domain.

The whole domain was divided into parts which were meshed separately, but in conjunction at the interfaces, with unstructured triangular grids. The outer rectangular domain was meshed in a coarser manner, while more caution was taken for an inner rectangle that surrounded a distance upstream and downstream of the turbine. A denser non-conformal grid was generated for the rotational domain, where the grid spacing at the interface was alternated between the meshes. Smaller circle domains were placed around each airfoil to enhance the grid generation around the blades. Different meshes were generated for a grid independence study, where the grid spacing on the airfoils was varied between 1.5 mm, 3 mm, 10 mm and 20 mm. In Figure 3.3 the grid configuration for the different parts can be seen. Quadrilateral layers with a first cell height of 0.01 mm were built around the airfoils and resulted in y^+ values of 1.3. Specific details of the meshes can be seen in Table 3.1.

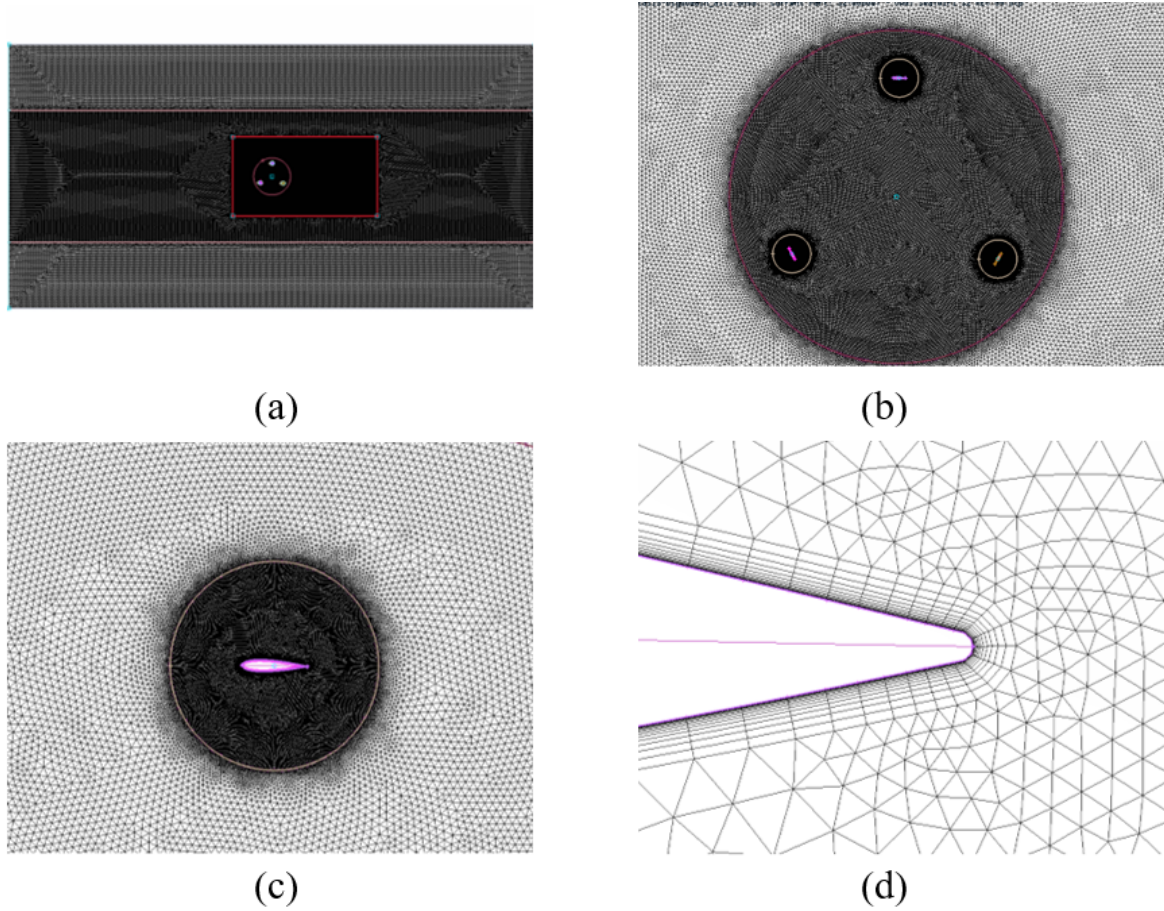


Figure 3.3: Grid configuration on some levels of the domain; (a) Whole numerical domain, (b) Rotating domain with refined mesh, (c) Smaller circles with refined mesh around each airfoil, (d) Close-up of the trailing edge of one blade.

Table 3.1: Differences between the four constructed meshes.

Parameter	Coarse	Medium	Fine	Extra fine
Cell size on blade [mm]	20	10	3	1.5
Nodes on each airfoil	284	548	1746	3656
Cell size on rotating domain [mm]	1000	700	300	300
Total number of cells	321 598	604 650	1 090 326	1 345 654

3.2.2 Numerical settings

The $k-\omega$ SST turbulence model was used to solve the unsteady RANS equations. The SIMPLE algorithm was used for the pressure-velocity coupling and 2nd order scheme was used for discretization in time and space. The sliding mesh function with a rotational speed of 1.2 rad/s was used for the rotating domain. The numerical time step size was determined by equation 3.2, where the increment of the azimuthal angle was 0.5° per time step. The uniform inlet velocities were set according to the free stream velocity at the heights mentioned in section 3.1.1. The turbulence conditions were specified as 5 % turbulent intensity and 10 % turbulent viscosity ratio.

The residuals together with the torque coefficient per azimuthal angle, according to equation 3.3, were used to determine the solution convergence. When the torque coefficient for all azimuthal angles varied less than 1 % compared to the result obtained during the previous revolution, the solution was considered converged.

$$\Delta t = \frac{2\pi deg}{360\omega} \quad (3.2)$$

$$\frac{C_T^{(n)}(\theta) - C_T^{(n-1)}(\theta)}{C_T^{(n-1)}(\theta)} < 0.01 \quad (3.3)$$

4

Results

This chapter presents the results from the wind profile generation and the case set-up for the 2D simulations. Thereafter, the result of the turbine performance for the velocity gradients are demonstrated.

4.1 Generation of a gradient wind profile

The three different methods for velocity profile generation are compared in Figure 4.1. They were all based on the known free stream velocity of 11 m/s at the height of 35 m.

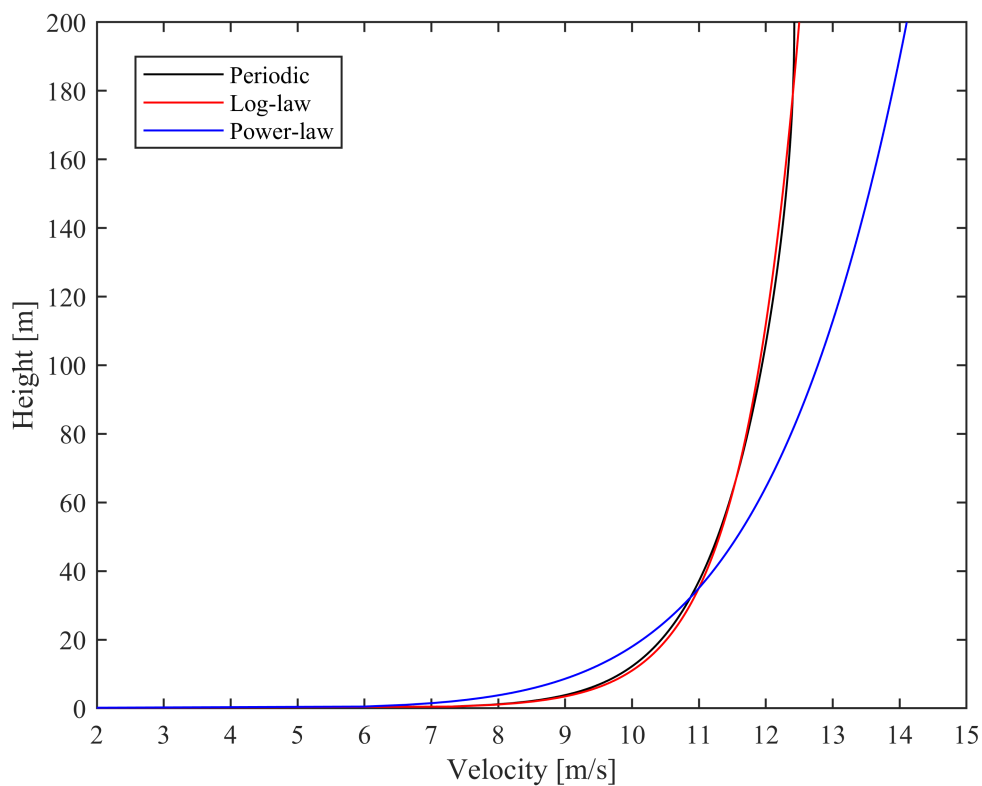


Figure 4.1: Comparison of wind profiles generated by three different methods.

4. Results

The black curve illustrates the behaviour of the velocity profile generated by the wall shear stresses in the periodic simulation. The red curve illustrates the velocity profile generated from the logarithmic law formula and it compared well with the periodic simulation. Thus, the calculated friction velocity was concluded to be accurate enough to contribute to a realistic velocity profile.

The blue curve, which illustrates the velocity profile generated by the power law equation, did not compare well with the periodic velocity profile. Hence, it failed to represent a realistic velocity profile and was excluded from the study.

The friction velocity was used to calculate the velocities at seven additional heights, seen in Table 4.1.a. Over the blade height, which reached from 10 m to 50 m above the sea level, the velocity increased with 1.38 m/s. Since the rotational velocity of the turbine was fixed, this resulted in decreased tip-speed-ratio with increased free stream velocity. Over the blade height the tip-speed-ratio changed from 3.04 at the lower tip to 2.66 at the upper tip.

A velocity profile was also derived based on a free stream velocity of 8 m/s at 35 m. For this free stream velocity the friction velocity was calculated to 0.257 m/s and the rotational speed of the turbine was 0.96 rad/s, according to Figure 2.2. The derived velocities and tip-speed-ratios for the different heights are given in Table 4.1.b. By comparing the two tables, it could be seen that the tip-speed-ratios differed between the cases and the tip-speed-ratios were higher for the case with 8 m/s at hub-height.

Table 4.1: Derived velocities and tip-speed-ratios for two different free stream velocities at hub-height.

(a) Velocities based on 11 m/s at 35m.

Height [m]	Velocity [m/s]	λ
10	9.92	3.04
20	10.52	2.86
30	10.86	2.77
35	11.00	2.74
40	11.11	2.71
50	11.30	2.66
60	11.46	2.63
70	11.59	2.60

(b) Velocities based on 8 m/s at 35m.

Height [m]	Velocity [m/s]	λ
10	7.21	3.33
20	7.65	3.14
30	7.90	3.04
35	8.00	3.00
40	8.08	2.97
50	8.22	2.92
60	8.34	2.88
70	8.43	2.85

4.2 Case set-up

The quality of the meshes was evaluated by comparing the averaged power coefficient for the last revolution. The deviating parameters between the meshes were the grid spacing on the airfoils and at the boundary of the rotating domain. The grid spacing on the airfoils drastically affected the results and the deviation in Cp_{avg} between the meshes is described in Table 4.2. The deviation in Cp_{avg} between the coarse and medium mesh was 12.7 %. The coarse mesh with a grid spacing of 20 mm underestimated the power coefficient and had difficulties to fulfill the convergence criteria given in equation 3.3. Thus, with a grid spacing of 20 mm the physics at the airfoil could not be properly resolved. The medium mesh, with a grid spacing of 10 mm, compared quite well with the finer mesh with 3 mm grid spacing. The difference in power coefficient between the medium mesh and the fine mesh was 5 %, where the finer mesh predicted higher values. Both meshes had stable numerical solutions which converged after the 8th revolution. Thus, a grid spacing of 10 mm on the airfoils should be enough to describe the physics around the airfoils. When comparing the fine mesh with a grid spacing of 3 mm to the extra fine with 1.5 mm spacing, negligible difference was observed. Therefore, a grid spacing of 3 mm was decided to be optimal for the study.

Table 4.2: Deviation in the power coefficient for meshes with different refinement of cells.

Comparison between meshes			
	Coarse	Medium	ΔCp
Nr of cells	321 598	604 650	12,7 %
	Medium	Fine	ΔCp
Nr of cells	604 650	1 090 326	4,8 %
	Fine	Extra fine	ΔCp
Nr of cells	1 090 326	1 345 654	0,1 %

The stability of the solution was determined by the residuals and the convergence criteria given in equation 3.3. The results showed that the convergence criteria was full-filled after the 8th revolution and therefore values for outputs were taken at the 9th revolution. The history of change of the averaged power coefficient for a number of revolutions are shown in Figure 4.2 and it could be seen that after nine revolutions no significant changes occurred for the Cp_{avg} .

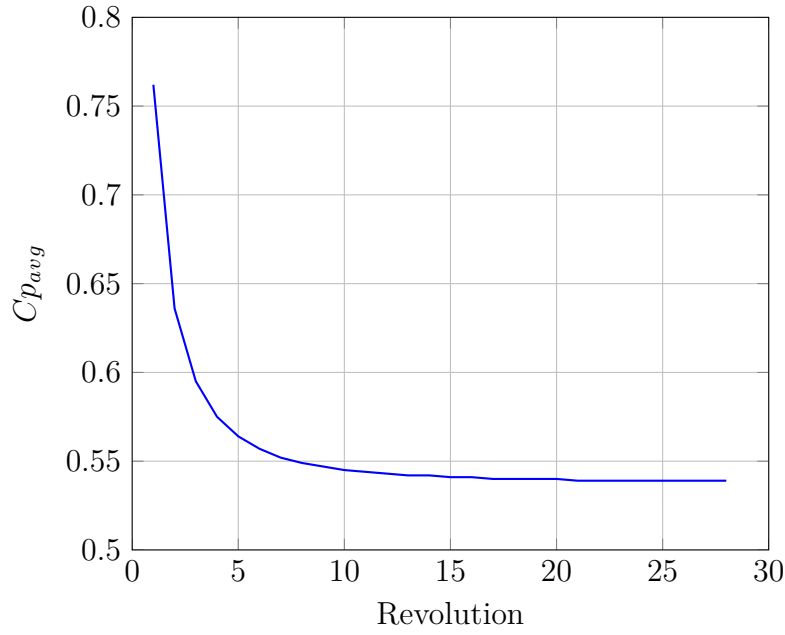


Figure 4.2: History effect of the averaged power coefficient.

Thereafter, the choice of azimuthal increment per time step was evaluated by comparing the average power coefficient for the last revolution for two different time step sizes. For the reference case the azimuthal increment was 0.5° rotation per time step, which was equal to a time step size of $7.25 \cdot 10^{-3}$ s. To evaluate if the increment was acceptable it was compared to $1/15^\circ$ azimuthal increment per time step, which was equal to a time step size of $9.7 \cdot 10^{-4}$ s. The resulting difference in Cp_{avg} for the 9th revolution was only 0.17 %, see Table 4.3. By that, an azimuthal increment of 0.5° per time step was concluded to give accurate results for the study and therefore used in the studies.

Table 4.3: Deviation in power coefficient for different azimuthal increments per time step.

	Time step size		
Azimuthal increment	Base case	Small	ΔCp
$\Delta\theta$ [$^\circ$]	0.5	1/15	
Δt [s]	$7.25 \cdot 10^{-3}$	$9.7 \cdot 10^{-4}$	
Cp_{avg}	0.5895	0.5885	-0.17%

4.3 The effect of a gradient velocity profile

To clarify how the incident velocity gradients affected the rotor output, the results from all 2D simulations were assembled in the same graphs. First of all, the averaged torque coefficients for the two free stream velocities were compared in Figure 4.3. Clearly the torque coefficient for the free stream velocity of 8 m/s continued to increase for increased height, while for the free stream velocity of 11 m/s the maximum torque coefficient was reached at 35 m. The decreased torque with height was a result of reduced tip-speed-ratio.

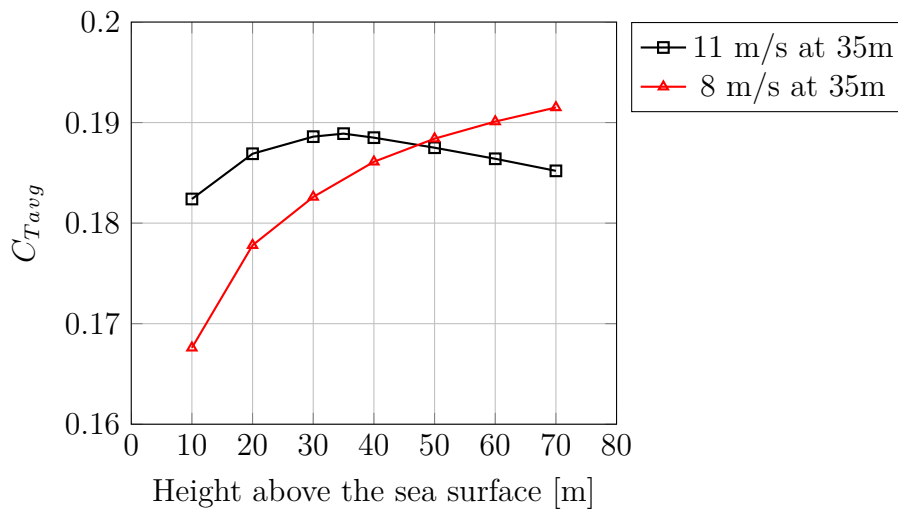


Figure 4.3: The torque coefficient for the different free stream velocities at different heights.

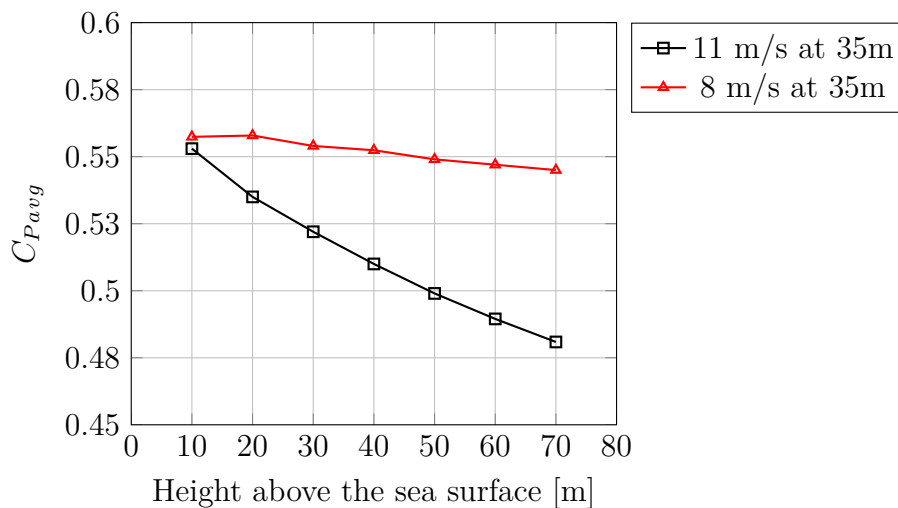


Figure 4.4: The resulting C_{Pavg} for the different free stream velocities at different heights.

4. Results

From the torque coefficient the averaged power coefficient for each height were calculated and the results were compiled in Figure 4.4. The curves showed how the efficiency responded to a change in tip-speed-ratio. First it could be noted that the $C_{p_{avg}}$ was higher for the tip-speed-ratios that were based on the free stream velocity of 8 m/s at hub-height. It could also be noted that for both cases the power coefficients were decreasing with height. However, a more drastic decrease was observed for the case based on 11 m/s at 35 m. The efficiency of the power extraction decreased due to that the rotational speed of the turbine was not optimal for the free stream velocity.

4.3.1 Power output based on a free stream velocity of 11 m/s

The possible power extraction for all heights were compiled in Figure 4.5. The curve decreased with height, which was a result of ineffective power extraction due the nonoptimal tip-speed-ratio. The total power output that could be generated by the wind turbine was obtained by integrating the area under the curve. For the current rotor design, where the height of the turbine blades was 40 m and ranged from 10 m to 50 m above the sea surface, the power output was integrated by the red area under the graph in Figure 4.5. The result declared that for a free stream velocity of 11 m/s at 35 m the total power output would be 804 kW.

The calculated power output for a uniform wind profile with an inlet velocity of 11 m/s was 843 kW. Thus, the estimated power generation deviated with 5 % whether a uniform or gradient wind profile was used.

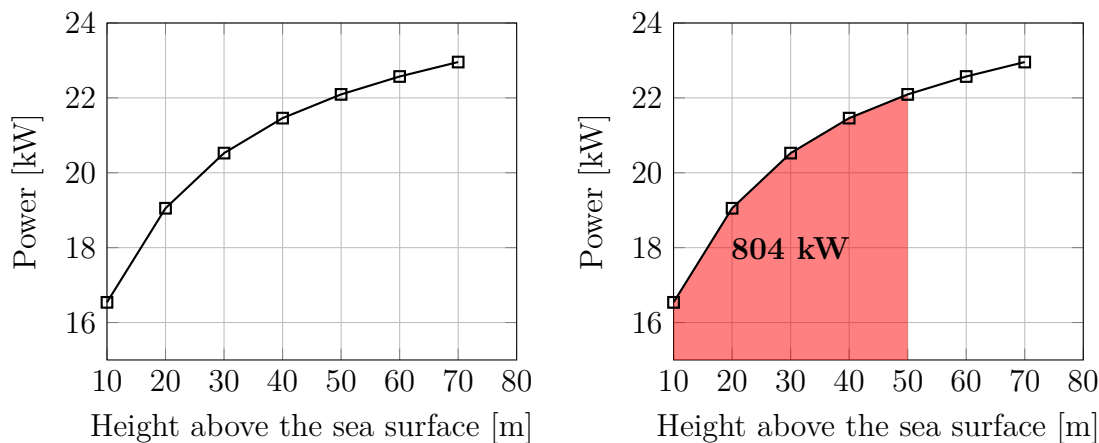


Figure 4.5: The left graph illustrates the calculated power at different heights. The right graph illustrates the total power output for the current rotor design.

The design options were evaluated by integrating the area under the curve for different boundaries. For a rotor position 10 meter higher up in the air, the power output was integrated between 20 to 60 m above the sea surface and resulted in 849 kW. See left Figure 4.6. For a rotor position 20 meter higher than current design, the total power was integrated between 30 m to 70 m above the sea surface and resulted in 879 kW, see right Figure 4.6. Both options resulted in increased power extraction compared to current rotor design, 5.6% and 9.3% respectively.

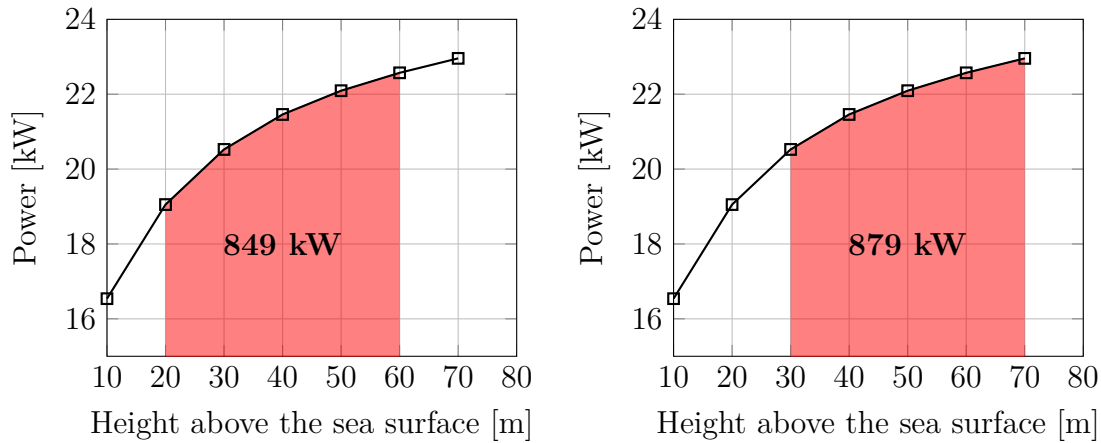


Figure 4.6: The graphs display the total power output for positioning the rotor 10 m higher (left) and 20 m higher (right) than current design.

The other alternative for optimizing the power extraction was to increase the height of the rotor blades i.e increasing the swept area. If the rotor blades would be 45 m tall, the swept area would be 2250 m² instead of 2000 m². The total power output was calculated by integrating the area between 10 m to 55 m above the sea surface and resulted in 915 kW. For rotor blades with a height of 50 m, the swept area would be 2500 m². The blade would range between 10 m to 60 m above the sea surface and the total power output was calculated to 1.03 MW. The possible power extraction were increased with 14 % and 28 % respectively compared to the current design and the results are illustrated in Figure 4.7.

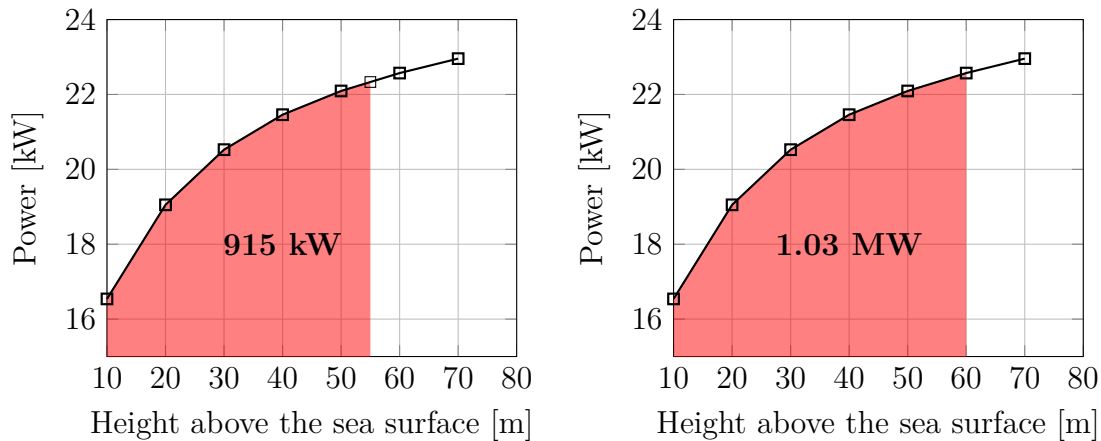


Figure 4.7: The graphs display the total power output for 45 m tall (left) and 50 m tall (right) rotor blades.

4.3.2 Power output based on a free stream velocity of 8 m/s.

The results for the cases based on a free stream velocity of 8 m/s at 35 m were compared in the same manner. The power curve that corresponded to the possible power extraction at each specific height was compiled in Figure 4.8. For the current rotor design

4. Results

the possible power output was calculated to 329 kW. The design options resulted in similar percental increases in power extraction as for the previous case. When the rotor was positioned 10 m higher up, so the blades ranged between 20 m to 60 m, the power output was 354 kW, see Figure 4.9. For a further increase in rotor position, such as the blades ranged between 30 m to 70 m resulted in 372 kW. The percental increase from current design was 7.6 % and 13 % respectively. The second design option also showed similar results; the power output for 40 m tall blades was calculated to 376 kW and for 50 m tall blades 424 kW. Hence, the increased blade height resulted in 14 % and 29 % more power output than the current design. See Figure 4.10.

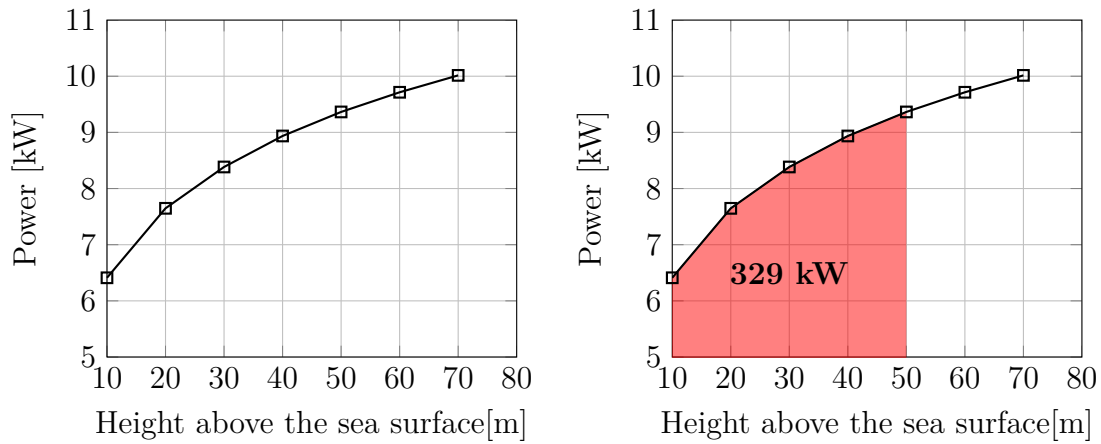


Figure 4.8: The graphs displays the power curve for a free stream velocity of 8 m/s (left) where the total power output for the rotor is given by the area under curve (right).

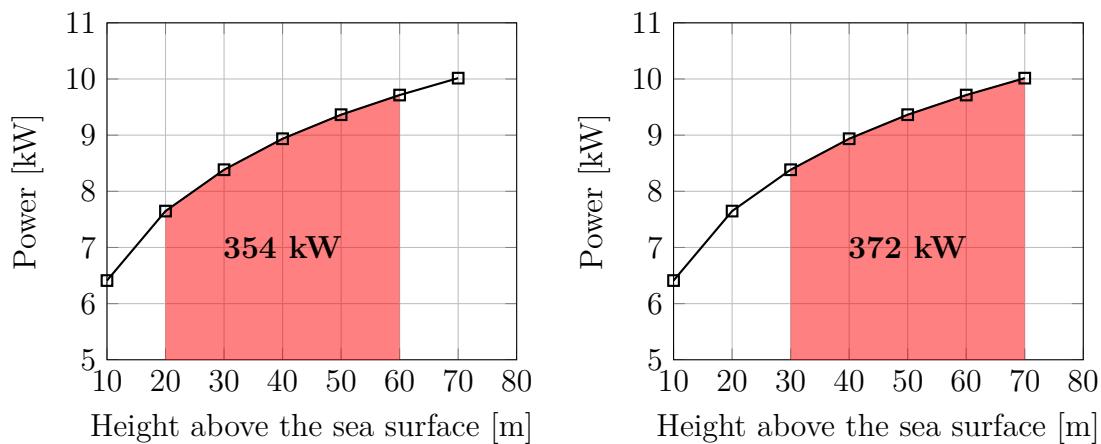


Figure 4.9: The graphs displays the total power output for positioning the rotor 10 m higher (left) and 20 m higher (right) compared to current design.

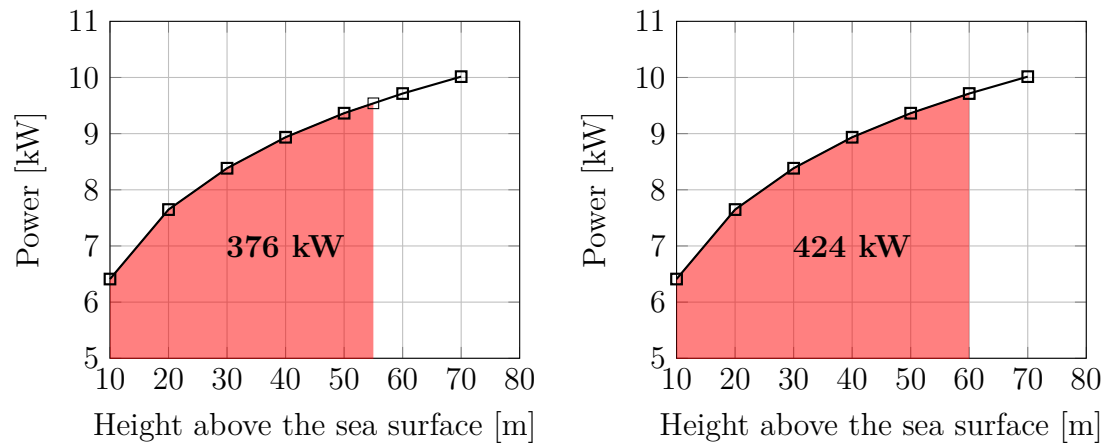


Figure 4.10: The graphs displays the total power output if the rotor blades would be 45 m (left) and 50 m (right).

4.3.3 Forces acting on the blades

To get a deeper knowledge of how the power output was affected by the tip-speed-ratio, the forces acting on the blades were examined for three cases which were based on the free stream velocity of 11 m/s at 35m. Since the free stream velocity increased with height, the relative velocity, angle of attack and the forces acting on the blade differed as well. Figure 4.11 illustrates how the angle of attack varied with height i.e for different tip-speed-ratios.

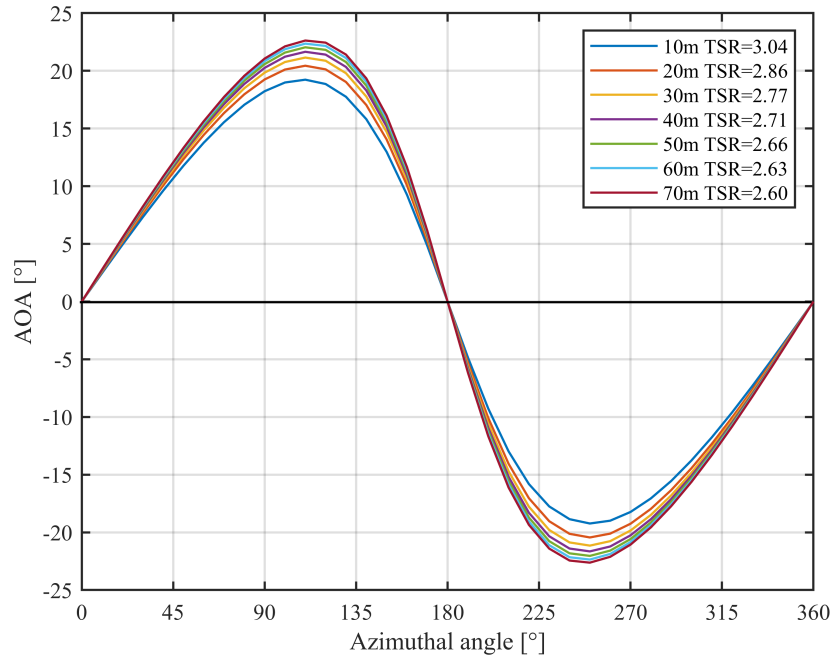


Figure 4.11: Variation in angle of attack during one blade revolution for different tip-speed-ratios.

The lift coefficients for the three cases, which represented the velocity gradients appearing at the heights of 20 m, 50 m and 70 m above the sea surface were compiled in Figure 4.12. The figure illustrates how the lift coefficient for one blade varied with azimuthal angle. In Figure 4.13 the lift coefficient was plotted against angle of attack. The maximum lift coefficient was reached at an angle of attack of 20° - 22° (depending on the relative velocity) which corresponded to an azimuthal angle of 100 - 110° . After the maximum lift coefficient was reached, the behaviour for the downstroke motion deviated between the three cases. For the lower tip-speed-ratio, especially the black line, the lift coefficient was rapidly reduced for a small change in angle of attack. It could also be seen that the lift coefficient was notable higher for the case with higher tip-speed-ratio, the red curve, on the downstroke motion between the angle of attack of 20° to 0° . The behaviour was explained by the contour plots of vorticity magnitude in Figure 4.16. Some disturbances were noted at an angle of attack of -20° , which correspond to an azimuthal angle of 220° . The disturbances originated from the blade cutting through the rotor wake formed by vortices from the other blades and thus resulted in an instantaneous change in the lift coefficient.

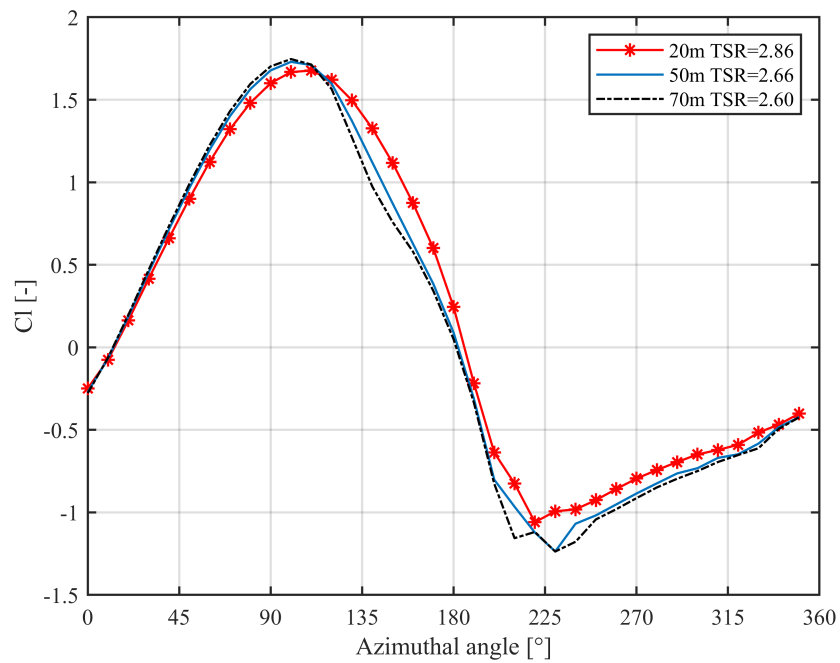


Figure 4.12: Lift coefficient for one blade versus azimuthal angle of attack for three different tip-speed-ratios.

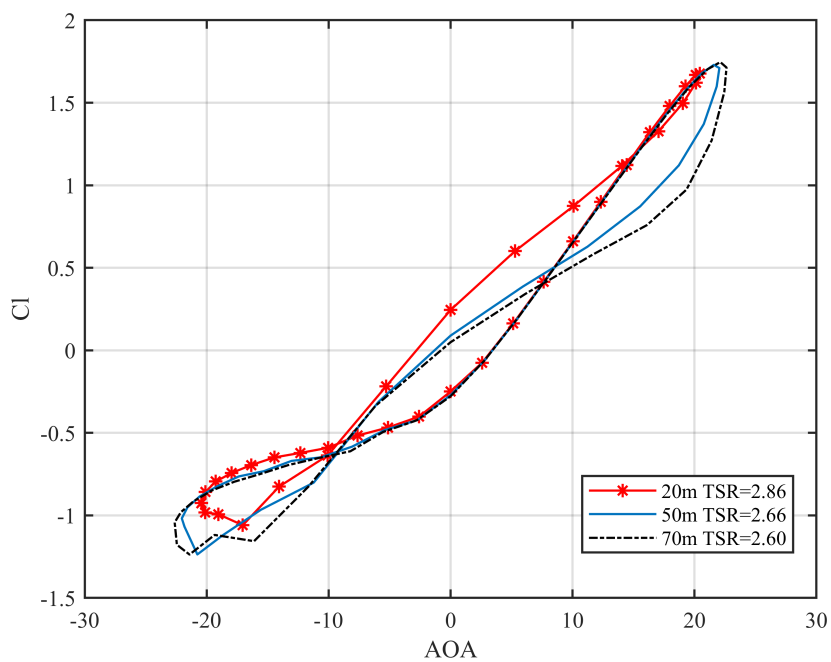


Figure 4.13: Lift coefficient for one blade versus angle of attack.

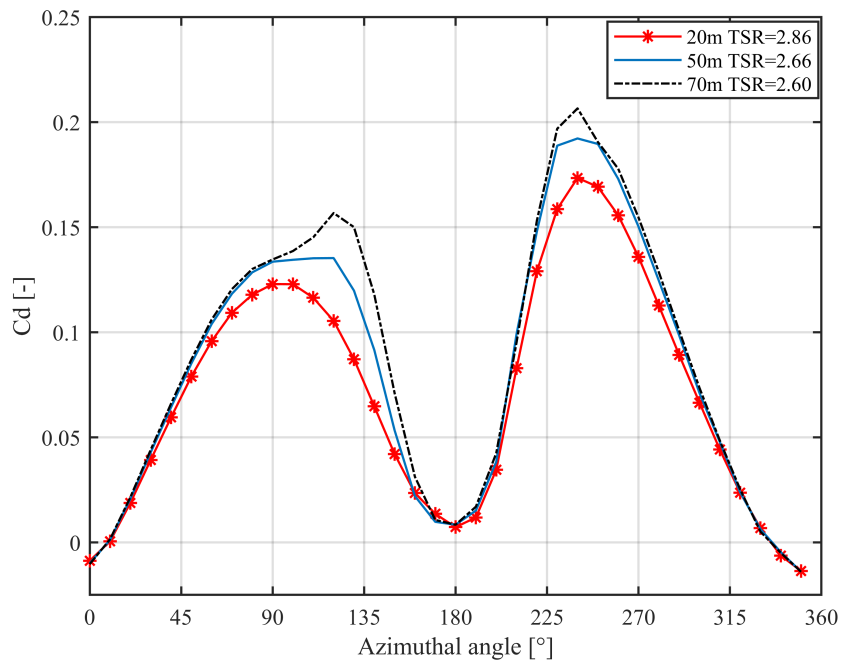


Figure 4.14: Drag coefficient for one blade over one revolution.

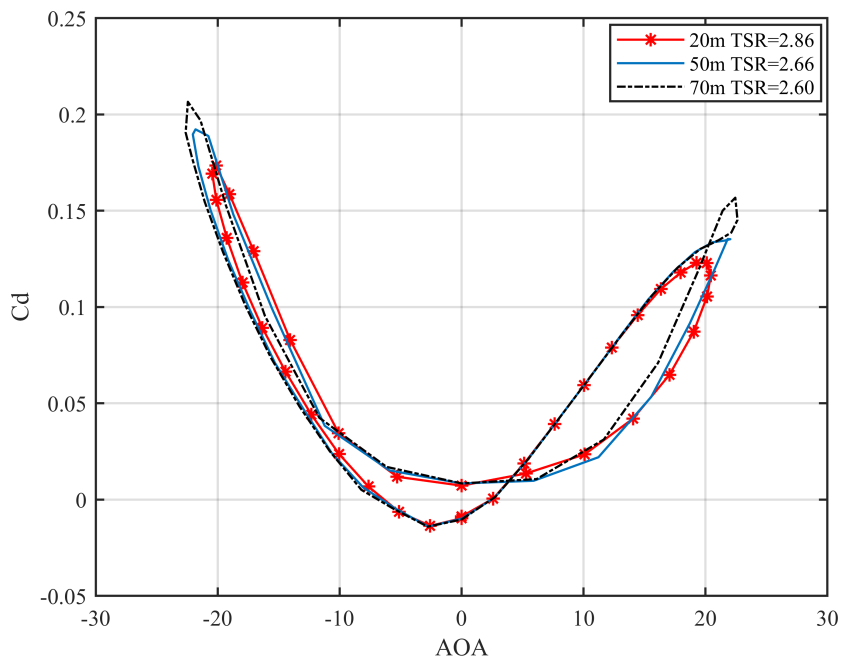


Figure 4.15: Drag coefficient for one blade versus angle of attack.

In Figure 4.14 the drag coefficient for the three cases was plotted against azimuthal angle and the behaviour was notably different. Largest value of the drag coefficient was observed for a free stream velocity which corresponded to a height of 70 m above the sea surface i.e the case with lowest tip-speed-ratio. For this case additional peaks appeared between 120-135° and at 230°. This behaviour was explained by the contour plots of vorticity magnitude in Figure 4.16. In Figure 4.15 the drag coefficient was plotted against angle of attack and it deviated considerably between the three cases at -20° and 20°.

To understand the large deviations in the lift and drag coefficients between the cases, contour plots of the vorticity magnitude were compared in Figure 4.16. They illustrate how the flow separation behaved for the three different tip-speed-ratios at the same azimuthal angle. In figure a, b and c the azimuthal angle was 130° and the trailing edge stall was observed, but the separation of flow was more severe for the lower tip-speed-ratios i.e increased free stream velocity. More stall reduced the lift and increased the drag force. For the lower tip-speed-ratios the unsteady flow resulted in build-up of trailing edge vortices which were later detached. While for higher tip-speed-ratio the flow was more or less attached to the airfoil during the whole revolution.

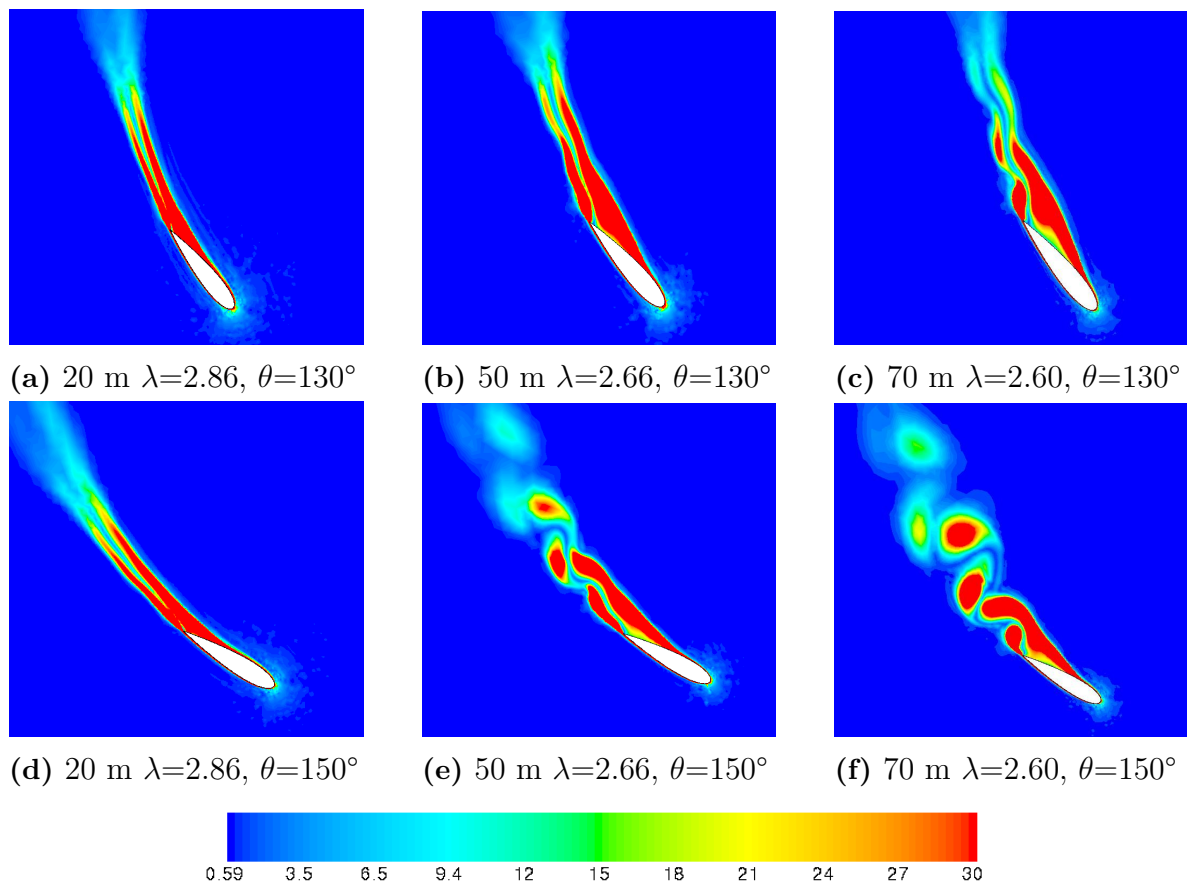


Figure 4.16: Contour plots of vorticity magnitude illustrating the flow separation for different tip-speed-ratios at an azimuthal angle of 130° and 150°.

5

Discussion

By comparing the three different methods for a velocity profile generation, the results showed that the logarithmic law performed better than the power law formula and was therefore used in the study.

The numerical model was set up by evaluating different meshes and a time step size of 0.5° azimuthal increment per time step was concluded to be sufficiently good to give accurate results. However, the domain size, time step size and grid size are parameters that could be further optimized to get a more accurate solution. This study has aimed to get accurate result for a reasonable computational time.

The velocity gradients for the different heights were derived for two cases, based on either 8 m/s or 11 m/s at hub-height. The velocities represented a specific height and were used as inlet velocities in the 2D simulations. The resulting power outputs for each case were compiled in to a power curve and by integrating the area under the curve the total power output was calculated. For both cases the curve decreases with height which was a result of inefficient power extraction. It depended on the rotational speed of the rotor which was nonoptimal for the increased free stream velocity that appeared with increased height.

Regarding the design options, the first alternative (to elevate the rotor position) did not result in a significant larger power extraction since the rotational speed limited the power efficiency for increased free stream velocity. Nevertheless, changing the rotational speed so the tip-speed-ratio would be more optimal would give more favourable results. However, to elevate the rotor position contradicts two of the major advantages with the VAWT construction, namely the low center of mass and the simplified maintenance. Instead, a more promising alternative would be to increase the swept area i.e the height of the rotor blades; which resulted in a substantial increased power extraction. Of course it is also a matter of construction limitations and production costs.

Also to be mentioned, this power extraction is only an indication of the capacity of the current wind turbine design, a more realistic power estimation would require information about site specific Rayleigh distribution data of the wind speed over time.

Either way, the study showed that the higher blade position resulted in increased forces acting on the blades. The upper part of the blades got unfavourable low tip-speed-ratios which in turn resulted in more flow separation and dynamic stall effects. This reduced the lift force and generated more drag. This is a short come of

the fixed blade design for all vertical axis wind turbines and thus inevitable. However, the rotational speed could be optimized such as the optimal tip-speed-ratio is achieved at the upper tip of the blades instead of at the hub-height.

The effect of wind shear contribution on the power calculations was evaluated by comparing the difference in power output for a uniform velocity of 11 m/s, compared to integrating the power curve for the gradient wind profile. The difference in estimated power output was 5%, where the uniform profile overestimated the output. The result may depend of the position of the measure point, since the blade ranged between 10-50 m above the sea level, the measure point positioned at 35 m is not in the middle of the blades.

6

Conclusion

To conclude, it is possible to use a uniform velocity profile to get an approximation of the possible power output for a vertical axis wind turbine. After all, the numerical model used in this project may give result that also deviates 5% compared to a more accurate solution. However, for a large-scale vertical axis wind turbine where the blade height ranges several meters, the forces acting over the blade deviates a lot because of the changed wind speed and nonoptimal tip-speed-ratio. The study have pointed out the significance of the tip-speed-ratio, where a small change in tip-speed-ratio resulted in dynamic stall effects. Therefore, when only using a uniform wind profile with optimal tip-speed-ratio the contributions from lift, drag and stall effects get unnoticed.

The study showed that the most profitable design option would be to increase the swept area instead of the rotor position. It would be desirable to make a full 3D model to validate the 2D method and see how the end effects of the blades affect the predicted power output and forces acting on the blades. But, that is left for future studies.

Bibliography

- [1] S. Emeis. *Wind Energy Meteorology. [electronic resource] : Atmospheric Physics for Wind Power Generation*. Green Energy and Technology. Cham : Springer International Publishing : Imprint: Springer, 2018., 2018.
- [2] E. Hau. *Wind Turbines: Fundamentals, Technologies, Application, Economics*. Springer, Berlin, Heidelberg, 2006.
- [3] M. Sathyajith. *Wind energy: Fundamentals, Resource Analysis and Economics*. Berlin: Springer, 2006.
- [4] DNV GL. Recommended practice - environmental conditions and environmental loads. Technical report, DNV-GL AS, www.dnvgl.com, August 2017. DNVGL-RP-C205.
- [5] David C. Wilcox. *Turbulence modelling for CFD*. 3rd edition. DCW Industries, California, 2006.
- [6] L. Håkansson M. Mortensen R. Sudiyo B. B. Andersson, R. Andersson and van Wachem. *Computational Fluid Dynamics for Engineers*. 14th edition. Cambridge University Press, 2018.
- [7] J. Blazek. *Computational fluid dynamics. [electronic resource]: principles and applications*. 3rd edition. Amsterdam: Butterworth-Heinemann, 2015.
- [8] ANSYS, Inc. *ANSYS FLUENT 12.0 User's Guide*, 12 edition, 1 2009. RETRIEVED 2019-03-12.
- [9] B. Blocken A. Rezaeiha, I. Kalkman. Cfd simulation of a vertical axis wind turbine operating at a moderate tip speed ratio: Guidelines for minimum domain size and azimuthal increment. *Renewable Energy*, 107:373–385, July 2017.

